The On-orbit Optical Performance of the Space Telescope Imaging Spectrograph[a]

C. W. Bowers[b,d] B. E. Woodgate[b,d] R. A. Kimble[b,d] M. E. Kaiser[b,c,d] T. R. Gull[b,d] S. B. Kraemer[b,e]

G. F. Hartig[h]

D. A. Content[d]

D. C. Ebbets[f] D. Michika[f] J. F. Sullivan[f] R. A. Woodruff[f] M. Bottema[f,k]

D. J. Lindler[g] P. C. Plait[g]

C. Standley[j] N. R. Collins[i] R. H. Cornett[i] W. B. Landsman[i] E. M. Malumuth[i]

R. D. Robinson[e]

[c] Department of Physics and Astronomy,
The Johns Hopkins University, Baltimore, MD 21218
[d]Goddard Space Flight Center, Code 680, Greenbelt, MD 21077
[e]Catholic University of America, Washington, DC 20064
[f]Ball Aerospace and Technologies Corporation, Boulder CO 80301
[g]Advanced Computer Concepts, Inc, Potomac, MD 20854
[h]Space Telescope Science Institute, 3700 San Martin Drive,
Baltimore, MD 21218
[i]Raytheon/STX
[j]Adaptive Optics Associates, Cambridge, MA 02140

ABSTRACT

The Space Telescope Imaging Spectrograph (STIS) STIS operates from the ultraviolet to near infrared (115-1000nm) providing a general purpose, imaging spectroscopic capability. An internal, two mirror relay system corrects the spherical aberration and astigmatism present at the STIS field position. Low and medium resolution imaging spectroscopy is possible throughout the spectral range and over the 25 arcsecond ultraviolet and 52 arcsecond visible fields. High resolution (30-100,000) echelle spectroscopy capability is also provided in the ultraviolet (115-310nm). Target acquisition is accomplished using the STIS cameras, either UV or visible; these cameras may also be used to provide broad band imaging over the complete spectral range or with the small selection of available bandpass filters. A wide selection of slits and apertures permit various combinations of spectral resolution and field size in all modes. On board calibration lamps provide wavelength calibration and flat fielding capability. We report here on the optical performance of STIS as determined during orbital verification.

Keywords: STIS, HST, spectrograph, gratings, ultraviolet

1. INTRODUCTION

The Space Telescope Imaging Spectrograph (STIS) is an observatory level, axial instrument placed on board the Hubble Space Telescope (HST) in February, 1997 during STS-82. STIS replaced both the Goddard High Resolution Spectrograph (GHRS) and the Faint Object Spectrograph (FOS) and thus provides the primary Hubble spectroscopic

Correspondence should be referred to C. W. Bowers at bowers@stars.gsfc.nasa.gov

[a]Based on Observations with the NASA/ESA *Hubble Space Telescope*, obtained at the Space Telescope Science Institute, which is operated by the Association of Universities for Research in Astronomy, Inc. (AURA), under NASA contract NAS5-26555.

[b] Co-Investigator, STIS Investigation Definition Team

[k] Deceased

capability. STIS complements and extends the capabilities of these two first generation instruments principally by: (1) using two dimensional areal detectors for spatial imaging spectroscopy of up to 25" in the ultraviolet (115-310nm) and up to 52" in the visible/near-IR (310- 1100nm) at scales as small as 0.050" (2) allowing echelle spectroscopy over much greater simultaneous bandpass than the first generation instruments thus greatly increasing observational efficiency when extensive spectral coverage is necessary, (3) providing full field UV and visible camera capability for target acquisition and for scientific imaging using the small complement of available filters.

In this paper, we will summarize some of the optical performance characteristics of STIS, concentrating on results from in-flight measurements. Useful references for STIS optical performance include Woodgate et al.[1] for design aspects, Content[2] for grating testing and characterization, Kimble[3] for overall in-flight performance. A previous paper[4] gave a summary of optical performance based on the earliest in-flight results.

2. OPTICAL CONFIGURATION

Light entering STIS passes through a two mirror, ~1:1 correcting system based on the similar CO-STAR design. The corrector system removes the OTA spherical aberration, coma and astigmatism at the STIS field location and produces an intermediate focus at the spectrograph entrance slit plane. Any one of 64 apertures of various sizes and shapes, including some with bandpass or neutral density filters, can be inserted by appropriate commanding of the slit wheel. After passing the slit plane, the f/24 beam expands and is collimated by the off-axis, concave ellipsoidal collimator. The resulting beam is directed to the mode select mechanism (MSM) which contains a set of 21 optical components, including gratings, off-axis parabolic camera mirrors, a UV prism and flat fold mirror. Positioning a particular component into the collimated beam selects the STIS mode by re-directing the light toward one of the detectors either directly or through other intermediate, focusing optics.

The basic mode configurations are as follows. The ultraviolet modes (115-310nm), use either of two MAMA solar blind, photon counting detectors to cover a nominal 25" x 25" field. The CsI (FUV) or CsTe (NUV) photoemissive coatings define the primary detector passbands as 115-170nm and 115-310nm. While the NUV MAMA is primarily used from 165-310, the short wavelength sensitivity permits the incorporation of very broad pass camera modes and it may be used as a backup to the FUV MAMA. Each photon is located in a 2048x2048 grid (MAMA high resolution mode), though frequently the lower resolution 1024x1024 mode is used (low resolution pixels will be used throughout this paper unless specifically stated otherwise). Low and medium resolution spectrographic modes are provided with full 25" field coverage at nominal resolving powers of 1000 and 10000 at nominal focal ratios of f/86 and f/73. The low resolution modes incorporate off-axis parabolic gratings in Wadsworth mountings to provide the highest UV sensitivity within the STIS configuration. The medium resolution modes use plane gratings in a Czerny-Turner mounting. Both low resolution modes are capable of covering their entire passbands in a single exposure; the same coverage requires 11 (far UV) and 18 (near UV) settings for medium resolution spectroscopy. Medium and high resolution UV echelle modes are also provided with nominal resolving powers of 30000 and 100000 respectively. The nominal 0.2" long echelle slits provide order separation, though longer slits may be used if advantageous for a particular observation. A single, double pass prism is also included to cover the entire ultraviolet passband in a single exposure. Two off-axis parabolic mirrors, used with the FUV MAMA, provide 115-170nm direct imaging capability over the full UV field with or without filters located on the slit wheel. A third off-axis parabola is focused to the CsTe MAMA detector and is designed to be used with a filter. With it's broadband sensitivity, insertion of the SrF_2 filter for example produces an effective passband limited at low wavelengths to >130nm by the filter and at high wavelengths $\lesssim$310nm by the photocathode sensitivity.

The visible/near-IR band incorporates a 1024x1024 CCD detector. The optical paths for visible/near-IR modes use common elements, except for the selection of MSM optical element. All these modes incorporate an off-axis, ellipsoidal camera mirror producing a final focal ratio of about f/36. These modes include plane gratings to provide low (R=500-1000) and medium resolution (R=5000-10000) long slit spectroscopy in the 310-550nm and 500-1100nm ranges and over the 52" field at f/36. A flat transfer mirror provides a camera capability over the full 52"x52" field, the mode which is normally used for target acquisition. When used with an open aperture, the bandpass is defined only by the sensitivity of the CCD detector. [OII] 373nm and [OIII] 501nm bandpass filters are also included for this band as well as a long pass (λ>550nm) filter; all filters limit the field to abut 28"x50".

The gratings and mirrors were produced by several vendors to a tolerance of 0.011λ rms at 633nm or better, over any 20mm sub-aperture[2]. High efficiency $AlMgF_2$ coatings were applied at Goddard Space Flight Center (GSFC) and a program of contamination control and monitoring was instituted at both GSFC and Ball Aerospace.

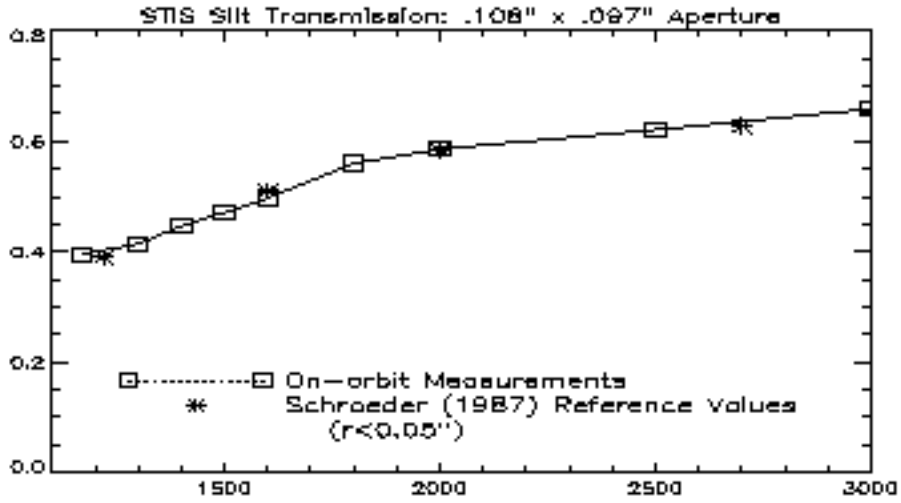

Figure 1. Performance of the STIS corrector in the ultraviolet. The measured transmission through the 0.108" x 0.097" aperture is shown with the expected OTA encircled energy for a radius of 0.05" from the pre-launch model of Schroeder.[5]

3. CORRECTOR - ALIGNMENT AND PERFORMANCE

The STIS corrector system consists of a spherical collimator which intercepts the beam from the OTA, and an anamorphic asphere which refocuses the beam at the slit plane. The spherical mirror produces an image of the telescope exit pupil on the asphere; decentration of this pupil at the asphere produces a primarily comatic image. The residual spherical aberration of the OTA is corrected as well as coma and astigmatism at the nominal STIS field point, 5.07' off axis. Both components were manufactured by Tinsley Laboratories, Inc., to an accuracy of 0.004λ rms at 633nm. Their performance at 633nm was validated at Ball Aerospace during gound testing by the Goddard Independent Verification Team and, at a system level, using the refractive aberration simulator (RASHOMS) at Ball Aerospace. The spherical corrector mirror is mounted on a mechanism which permits focus adjustment through $\pm$5 mm and tip/tilt adjustment through $\pm$32'. These adjustments compensate for the expected small OTA/STIS mis-alignment.

On-orbit alignment was performed in two steps: coarse alignment using images obtained with the CCD camera and fine alignment in the ultraviolet. The goal of alignment was to produce the maximum concentration of light at the spectrographic entrance plane; transmission through the nominal 0.1"x0.1" aperture was used as a measure of concentration. Co-alignment of all modes was performed pre-flight; individual modes cannot be separately aligned in flight. The results of the alignment procedure are summarized in Figure 1 where aperture transmission is compared to the pre-flight model of expected OTA (without STIS) performance[5]. The stars show predicted OTA encircled energy at 0.05" radius, essentially coincident over the full ultraviolet range with our measurements at the STIS slit plane.

4. LONG SLIT SPECTROSCOPIC MODES

4.1. Spectroscopic Resolution

Measurements using the on-board Pt/Ne calibration lamps have been made after launch to verify the spectral resolution of the primary, long slit spectroscopic modes. Table 1 shows these results, along with some other basic mode parameters. In all cases, the nominal two pixel wide long slits were used, 52" x 0.050" for the MAMA modes and 52" x 0.100" for the CCD modes. Uniform illumination across the slit width is produced by the on-board calibration lamps for these measurements. Resolving power has been determined using the best Gaussian fit fwhm to the line profiles. The resolving power values shown include variations throughout the bandpass and across the field. At nearly all modes, over the full field, the nominal resolution targets have been achieved in flight.

Table 1. Spectral resolution of the primary, long slit, science modes. Each mode is shown with the corresponding detector, nominal bandpass, bandwidth per exposure, number of exposures to cover the full bandpass, dispersion, measured resolving power and where the measurement was obtained. All measurements were with nominal, two pixel wide slits, 52" x 0.050" for MAMA modes and 52" x 0.100" for CCD modes.

Mode	Detector	Nominal Range (Å)	Å/Exp	Exp/Band	Å/pix	Resolving Power	Data Source
G140L	FUV MAMA	1150-1700	597	1	0.583	950-1400	Flight
G230L	NUV MAMA	1650-3100	1583	1	1.55	500-960	Flight
G230LB	CCD	1672-3077	1405	1	1.37	700-1050	Flight
G430L	CCD	3050-5500	2809	1	2.75	500-980	Flight
G750L	CCD	5500-10000	4993	1	4.88	560-760	Flight
PRISM	NUV MAMA	1150-3100	>1950	1	0.47-0.48	1200-31	Ground
G140M	FUV MAMA	1150-1700	54.3	11	0.0530	7800-19200	Flight
G230M	NUV MAMA	1650-3100	89.2	18	0.0872	8200-20600	Flight
G230MB	CCD	1650-3100	154	12	0.151	5200-11200	Flight
G430M	CCD	3050-5500	283	10	0.277	4900-10100	Flight
G750M	CCD	5500-10000	567	9	0.555	5100-10400	Flight

Figure 2 shows two typical examples of resolution maps, here obtained with the NUV MAMA for modes G230L and G230M. The absicissa is spectral dispersion (in pixels); spatial location along the slit length is indicated (in pixels) on the ordinate. The resolution values are the Gaussian fwhm in pixels. Nominal resolution goals were about 2.5 pixels. The low resolution mode (G230L) has nearly uniform resolution along the slit of about 1.8-2.0 pixels over about 70% of the slit length then decreases somewhat over the remaining 30% of slit length. Similar variations are seen in the comparable FUV mode, G140L. The medium resolution mode is more uniform with only about 10% decrease in resolving power at one end of the slit. The nominal two pixel slit projects to just 1.5 pixels in this mode and setting due to grating anamorphic magnification.

Similar resolution maps for other modes may be obtained[6,7]. Typical line profiles at selected field points and included energy ratios for many of the spectroscopic modes may be found in ISR 98-04[8].

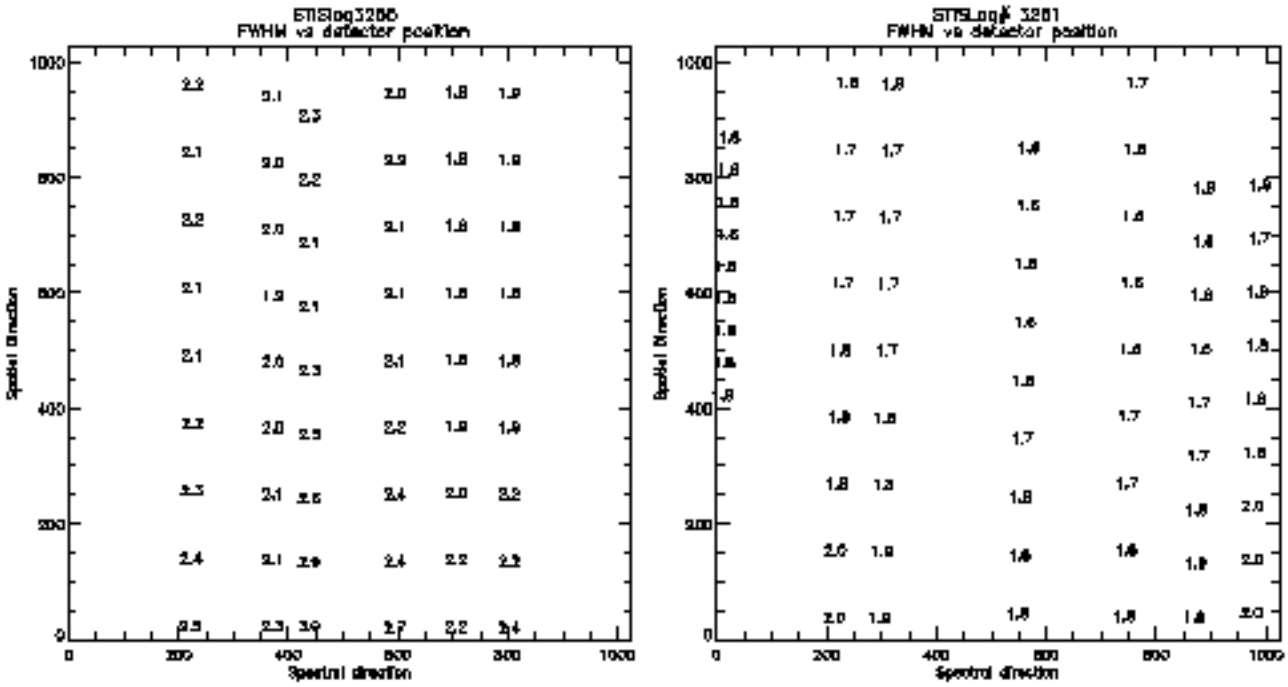

Figure 2. Full field spectral resolution of modes G230L, G230M. These maps demonstrate the spectral resolution along the long slits using the flight Pt lamps. The values are the Gaussian fwhm, in pixels, of selected spectral lines. The slit used was 52" x 0.050", uniformly illuminated by the lamps. The spectral (dispersion) and spatial directions are indicated; units are pixels.

4.2. Spatial Resolution and Stability

Spatial resolution of the primary spectroscopic modes, mostly obtained with the wide, 52"x2" slit, near field center is shown in figure 3. The plots show the Gaussian FWHM as a function of wavelength for observations obtained at various times over several months. The different symbols within each panel indicate measurements obtained on different days. Also shown are the two pixel sampling limits, about 0.05" for the UV modes and 0.10" for the visible/IR modes.

The upper panels of Figure 3 indicate similar trends of spatial resolution in the UV low and medium resolution modes. FWHM values of about 0.10" are obtained at the shortest wavelengths with improving performance to about 0.05-0.06" at the longest wavelengths. There are occasional discrepancies from the average values obtained with repeated measurements. The low resolution mode data of September 16, 1997 (open diamonds) is systematically worse than average; the medium resolution measurements near 150nm from July 25, 1997 are also discrepant. These differences are probably due to unusually large OTA secondary displacements (breathing). Such an effect causes a defocus and consequent lower resolution within STIS. Since an intermediate focus is formed at the STIS slit plane, appropriate slit selection can minimize resolution loss due to breathing, particularly relevent for maintaining spectral resolution.

One series of measurements with a bright stellar target using the nominal two pixel wide, 52"x0.05" slits in the low resolution UV modes has been obtained. The spatial resolution results, analyzed uding the MAMA high resolution mode, are shown as filled diamonds in the upper, left panel of Figure 3. A noticeable improvement is evident compared to the other data shown obtained with the 2" wide slit. The extent of the PSF at the slit plane broadens the line spread function formed when a wide slit is used; the narrow slit produces more of a slice through the PSF preserving it's compact core. There will be some loss of throughput as a more narrow slit is used however spectral purity is maintained. Pre-launch estimages of relative slit transmission are included in the STIS Observers Handbook (ref); ongoing slit transmission measurements will quantify the precise values.

The visible mode spatial resolution clusters around the two pixel limit of 0.1" as demonstrated in the lower panels of Figure 3. Mode G430M has systematic variations, at most settings, with the best spatial resolution consistently obtained at the longest wavelengths. This pattern suggests a field dependent aberration since the longest wavelengths

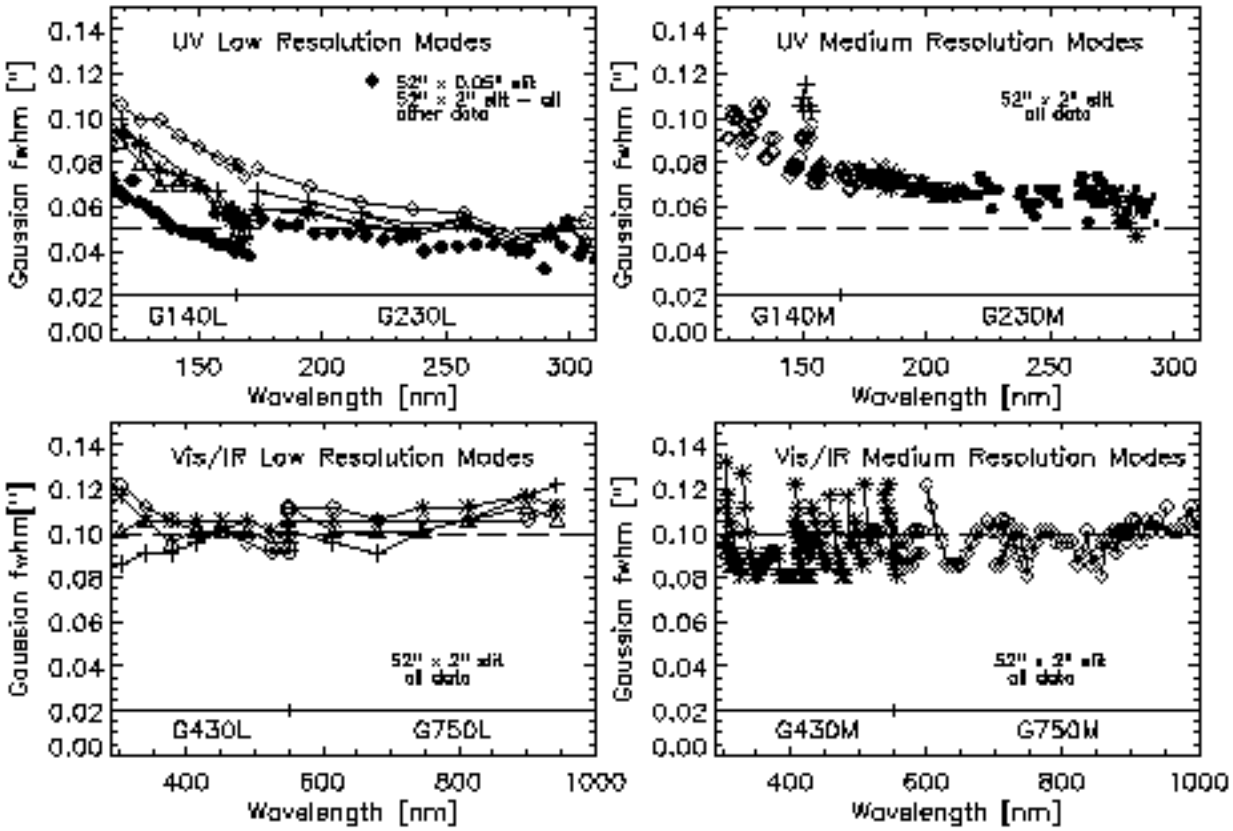

Figure 3. Spatial resolution and stability at field center in the primary, long slit modes. Each panel shows the best fit Gaussian fwhm in arcseconds for a number of different observations. All data were obtained using the wide, 52" x 2" slit. Note that two pixel, critical sampling (indicated by the horizontal, dashed line in each panel) is about 0.05" for the UV modes and 0.10" for the visible/IR CCD modes. Occasional excursions from the relatively tight distribution of widths are likely due to unusually large displacements of the OTA secondary (breathing).

at each setting are at the same relative field position. One example at a single setting of Mode G750M shows similar behavior but all other positions have less variation.

5. ECHELLE SPECTROSCOPIC MODES

Spectral resolution of the four, primary UV echelle modes is summarized in Table 2. These data were obtained using the onboard Pt/Ne lamps, uniformly illuminating the nominal, two pixel projected width slits, 0.200" x 0.060" for the medium resolution echelles (E140M, E230M) and 0.200" x 0.090" for the high resolution echelles (E140H, E230H). There is a small amount of resolution variation across the detector and this has been included in the results of Table 2; resolution maps of each mode are available[8]. The resolving power of the E140M echelle exceeds its design, NUV twin, E230M, due to the late substitution of an alternative, 45° echelle instead of nominal design 32° echelle grating. This change was made because of the substantially better efficiency of the alternative grating compared to the best of a number of gratings of the nominal design.

We note that the resolving powers cited in Table 2 do not represent the intrinsic limit of STIS but are slit limited values. Using the small, 0.100" x 0.025" slit the MAMA high resolution mode, and with the electron repelling voltage removed, a resolving power of 220,000 was demonstrated during ground testing in mode E140H[9]. A specially constructed mono-isotopic Pt lamp was used for this test to avoid blending of the Pt line profiles. Resolving powers between this value and the nominal value of 100000 may be obtained by using various combinations of intermediate size slits (S200x060 = 0.19"x0.05" for example) and repeller voltage on or off. Where appropriate, observers may take

advantage of this additional resolution capability, though they should confirm the availability of any non-standard configuration.

Table 2. Spectral resolution (low-res mode) of the primary echelle modes. Each mode is shown with the corresponding detector, nominal bandpass, bandwidth per exposure, number of exposures to cover the full bandpass, dispersion, measured resolving power and where the measurement was obtained. All measurements were with nominal, two pixel wide slits, 0.200" x 0.060" for the medium resolution modes and 0.200" x 0.090" for the high resolution modes.

Mode	Detector	Nominal Range (Å)	Å/Exp	Exp/Band	Å/pix	Resolving Power	Data Source
E140M	FUV MAMA	1150-1700	587	1	λ/91700	46000	Flight
E230M	NUV MAMA	1650-3100	808	2	λ/60000	29900-32200	Flight
E140H	FUV MAMA	1150-1700	202	3	λ/228000	99300-114000	Flight
E230H	NUV MAMA	1650-3100	277	6	λ/228000	92300-110900	Flight

5.1. Echelle Scatter

For proper determination of line profiles and to provide an accurate saturation zero point, it is important to account for the effects of grating scatter in high resolution spectroscopy. The scatter level from ruled gratings typically rises rapidly with shorter wavelengths, increasing the problems of spectroscopic absorption line analysis in the ultraviolet. With their deep grooves, echelle gratings are particularly subject to increased scatter. The grating evaluation and selection process for STIS[2] sought low scatter gratings as a primary goal. Detailed characterization of STIS grating scatter will be the subject of a forthcoming publication. Here we summarize our initial efforts to estimate and remove scatter from the STIS echellograms.

Cardelli et al[10,11] developed a semi-empirical method to correct for scatter in the GHRS high resolution modes with good success. Measured interorder to in-order light ratios for stellar targets were as high as 25% near 120nm, principally due to the low resolution cross dispersers. For STIS, the primary source of grating scatter in the echelle modes is the ruled, echelle gratings themselves with the contribution from the cross dispersers several orders of magnitude smaller. The magnitude of this effect and the small distance between orders causes comparable interorder scatter to that seen with GHRS: 20% for E140M and $\lesssim$8% for all other modes[12].

Figure 4 illustrates two sources of scatter in STIS echellograms: echelle scatter and detector halo. Figure 4 is a portion of an E230H echellogram of a Pt-Ne line lamp near 230nm. The image has been log-stretched and contrast adjusted to enhance the appearance of scattering features.

The echellogram orders are dispersed horizontally in this figure as evident from the distribution of slit images of numerous lines of the Pt lamp spectrum. Echelle grating scatter is apparent along the echelle dispersion direction, here tilted about 2.5° from the horizontally dispersed orders. This scattered light is seen to connect the same spectral feature in adjacent orders with a magnitude that tracks the echelle blaze function. The other "scatter" feature easily visible in the figure is detector halo caused by secondary electrons ballistically ejected from the surface of the detector microchannel plate (MCP). The distinct radial limit for the NUV detector is twice the photocathode/MCP separation. A much smaller halo is present in the Band 1 detector in which the photocathode is deposited directly onto the MCP and a repelling field is applied. Cross disperser scatter which would appear perpendicular to the echelle scatter is at such a low level as to not appear in the figure. Another source of diffuse light in STIS echellograms is due to OTA scatter, particularly in the far-UV, which is not seen in this Pt lamp exposure. The nominal slit length for echelle observations is 0.2" and limits OTA scatter to this extent. The nominal slit width (0.06" for medium resolution, 0.09" for high resolution) similarly limits the extent of the OTA PSF in the dispersion direction. When used with wider slits however, the OTA PSF provides another source of scatter, even for a point source, leading to absorption line filling.

From the non-local nature of echelle scatter, illustrated in Figure 4, it is clear that the simple method of subtracting adjacent interorder scatter from a spectrum will not generally properly correct for echelle scatter. For example, adjacent interorder light ten pixels from an order will originate from a point in the spectrum 230 pixels away for a

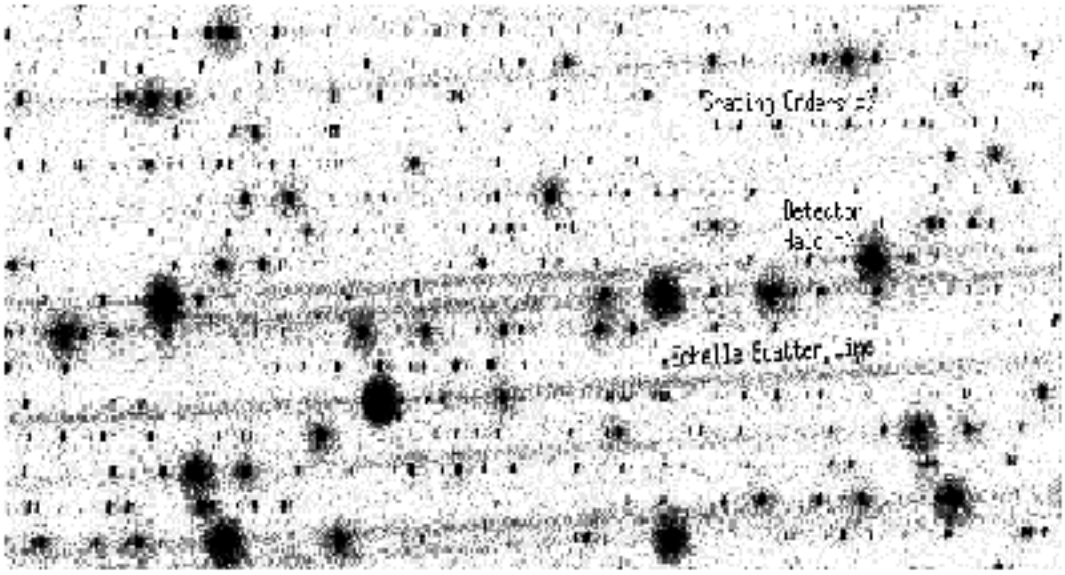

Figure 4. An echellogram illustrating some of the principal sources of scatter. The image has been log-stretched to enhance faint features. This image was obtained during ground testing of the E230H mode using an internal, Pt/Ne lamp with the 0.20" x 0.06" aperture. The region shown is near 230nm. The grating orders are dispersed horizontally; echelle scatter is in the echelle dispersion direction, about 2.5 degrees to the horizontal, and connects the same lines in adjacent orders. The detector halo is seen surrounding the brighter lines.

2.5° echelle to order tilt. Only for an intrisically flat spectrum will interorder subtraction provide a reliable scatter correction.

We are developing a two dimensional modelling routine to estimate and remove scatter from the STIS echelle modes. Our goal is to provide reliable estimates of both in-order and interorder scatter. While not directly necessary to produce an echelle scatter corrected spectrum, interorder scattered light is useful to provide an estimate of detector dark count, and for removal of any other diffuse scatter source such as may be present from longer wavelengths not directly included within the echellogram. It is hoped that this detailed modelling approach will allow compensation for the variety of observing conditions in which STIS may be used, naturally incorporating such variables as spectra obtained with different slits, spatially extended sources, and determining what size extraction box will obtain the optimal signal-to-noise. Here we outline our method and show some initial results.

The scatter corrected spectrum is obtained by directly subracting our model scatter estimate from the original, extracted spectrum. We do not seek the more difficult goal of deconvolving the extracted spectrum and so increasing it's signal-to-noise. Our scatter estimate should be smooth; subtracting it from the original spectrum should decrease the initial S/N only by the effect of lowering the overall number of counts, not by adding in noise generated by the algorithm. In addition, correct subtraction of scatter should result in zero net flux in saturated, broad absorption lines.

The data sources which are being incorporated include (1) measurements of echelle scatter, obtained in laboratory testing of the flight gratings as well as ground testing of the entire STIS instrument, (2) laboratory testing of the STIS UV MAMA detectors, and (3) modelling of the OTA PSF at the slit plane in STIS. All of these sources vary with wavelength and this variation must be incorporated in the final model. Several characteristically different spectra, obtained during ground testing and on orbit, are being used, to verify and improve the accuracy of all parameters.

Modelling is initiated by extracting the echelle spectrum an order at a time. A scaled version of the extracted order is used as an initial estimate of the pre-scattered flux. The various scatter models are then applied to this pre-scattered estimate, producing a model observed spectrum which is extracted and compared to the actual extracted spectrum. The pre-scattered flux is adjusted and the process is repeated until satisfactory agreement between model

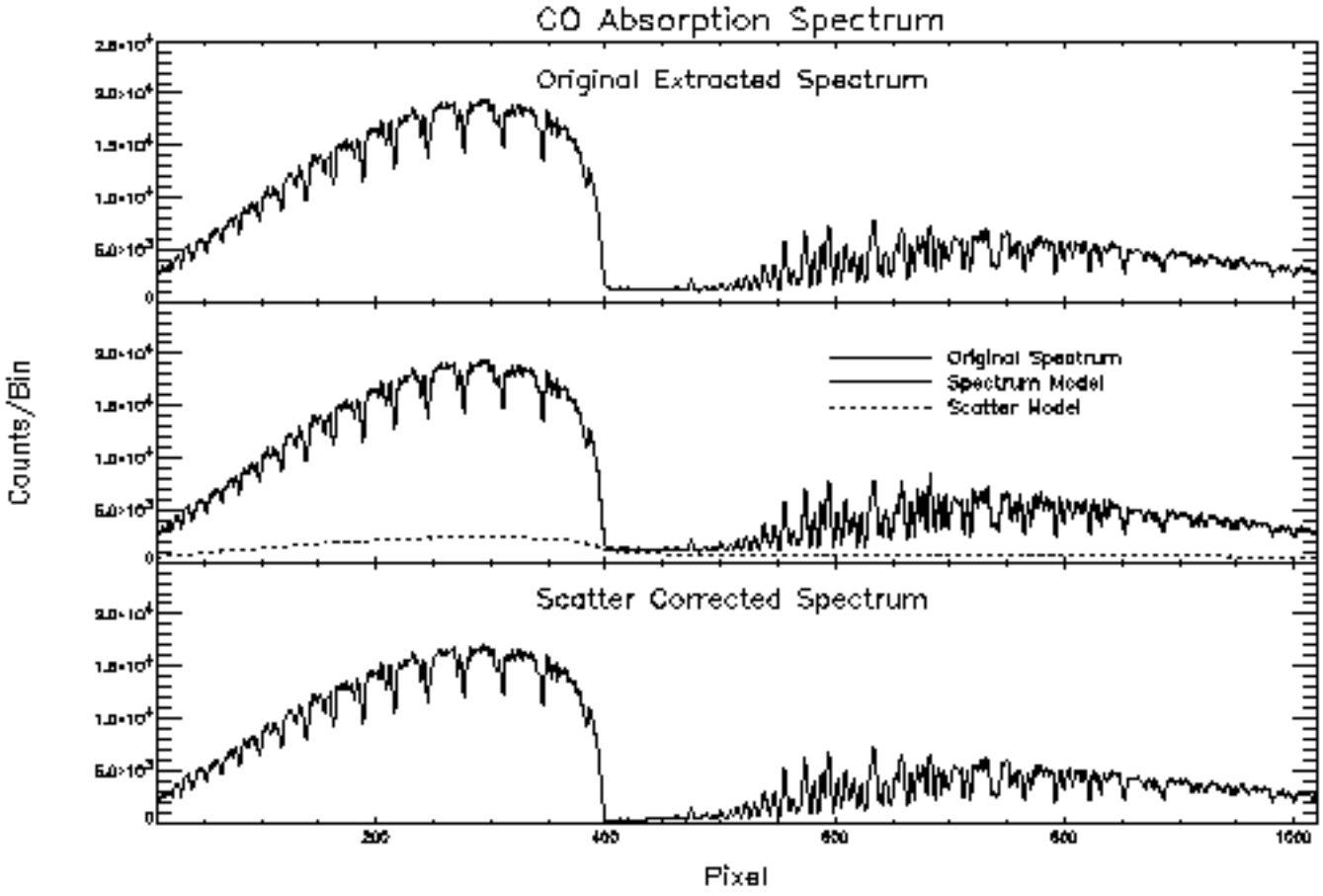

Figure 5. Steps in the scatter correction of echelle spectra. The top panel shows the original extracted spectrum from a single order near 150nm of the absorption spectrum of CO, obtained during ground testing of the E140M mode. The absorption edge is about 6% of the peak, continuum flux. The central panel shows the model of this spectrum, overplotted on the original, extracted spectrum; they are nearly indistinguishable in this figure. Also shown is the scatter estimate. The bottom panel shows the scatter corrected spectrum obtained by subtracting the scatter estimate from the original, extracted spectrum.

and data is obtained. At this final iteration the scattered light is tracked and subtracted to produce a scatter free spectrum and interorder spectrum.

An example of this process is shown in the three panels of Figure 5. The top panel shows the extracted spectrum of a single order from an absorption cell spectrum of CO obtained during system level ground testing in mode E140M, near 150nm. This spectrum was obtained with a uniformly illuminated slit 0.2"x 0.09". A strong continuum with numerous non-saturated absorption lines as well as a saturated absorption edge are apparent. The saturation level is raised about 6.6% of the maximum continuum primarily due to echelle scatter from the bright continuum. The iteration routine, just described was run on this spectrum incorporating echelle scatter and detector halo and convolved with the slit aperture. The center panel shows the original, extracted spectrum and overplotted, the modelled, observed spectrum obtained by scattering the iterated non-scattered flux. The actual and model spectra are nearly indistinguishable. Also shown in this panel by the dashed line is the estimated in-order scatter over the same extraction box. In this case, "scatter" was defined as light which originated beyond ± 3 pixels distant from a given pixel in the dispersion direction. The scatter estimate is smooth at about 1.2% of the continuum; the apparent underlying continuum longward of the absorption edge is seen to be almost entirely due to scattered light.

This modelling technique is now being refined and extended to successively correct each order and in all echelle

modes. Models of the variation of scatter sources with wavelength are being included. To correctly model the interorder scatter, additional spectral orders not falling on the detector must be included since they contribute significant scatter except near the center of each order. Additional on-orbit observations of astronomical sources are planned in the near future to provide calibration spectra for further testing.

6. CAMERA MODES

Camera modes are associated with each of the three STIS detectors. These are necessary for proper target acquisition and with the small complement of filters included, provide a valuable scientific imagery capability as well. A comparison of their limiting magnitude performance with WFPC2 is included in the accompanying paper[13] The performance of the FUV and NUV cameras with various filters is summarized in Tables 3 and 4. Considerable detail regarding the camera performance is available[14]. The encircled energy within a radius of 0.050" is presented and compared with reference values[5]. These latter reference values do not include the effects of any particular detector - they refer to optical performance alone.

Table 3. Performance of the STIS FUV camera modes as measured by the encircled energy within a radius of 0.050". The performance is given for each of the FUV filters using the astronomical targets indicated. Reference values are for expected OTA performance using the pre-flight model of Schroeder (1987)[5].

Filter	λ(c) [nm]	Target	Performance EE(r<0.050")	Reference EE(r<0.050")
A25	Clear	NGC6681	0.32-0.36 over full field	—
F25QTZ	λ>146	NGC6681	0.39-0.43 over full field	0.46 (155nm)
F25SRF2	λ>130	NGC6681	0.33-0.39 over full field	0.43
F25LYA	122	BPM16274	0.27 at field center	0.38

Table 4. Performance of the STIS NUV camera modes as measured by the encircled energy within a radius of 0.050". The performance is given for each of the NUV filters using the astronomical targets indicated. Reference values are for expected OTA performance using the pre-flight model of Schroeder (1987)[5].

Filter	λ(c) [nm]	Target	Performance EE(r<0.050")	Reference EE(r<0.050")
F25CN182	182	NGC6681	0.40-0.48 over 2/3 field, 0.30-0.40 over 1/3 field	0.55
F25C3	191	LS 749B	0.41 at a single, off-center field point	0.57
F25CN270	270	NGC6681	0.50-0.54 over 2/3 field, 0.40-0.50 over 1/3 field	0.62
F25MG2	280	BPM16274	0.51 at field center	0.63

Figure 6 consists of montages of log-stretched images from the FUV and visible/near-IR cameras. These were extracted from full frame, 1024x1024 pixel images of stellar clusters NGC6681 (FUV) and Omega-Cen (visible); the pixel location is indicated at the bottom of each sub-image. To the left and above each sub-image is the Gaussian fwhm in pixels in the vertical and horizontal directions. Each pixel projects to about 0.025" (UV) and 0.051" (visible) and the total field of each sub-image is about 1.3"x1.3" (UV) and 2.6"x2.6" (visible). Just to the right and above center of each UV sub-image is the encircled energy within a radius of 0.050". Cross sectional plots from corresponding horizontal cuts lie to the right of each montage. Figure 6 demonstrates the image quality of the FUV camera with broad band imagery. Both this and the similar NUV cameras were tipped toward the medium and echelle mode camera mirrors to insure full field high resolution spectroscopy, the primary STIS objective. Consequently the camera focal planes are tilted with respect to the detectors; the amount is sufficient to cause defocus at the edges of the field which is apparent in the FUV images. The bright, horizontal branch stars in the FUV image have characteristic temperatures of 8000-15000 K causing the flux weighted response to be maximum at about 120nm The

resulting halo evident in these log-stretched images is the result of the combination of STIS internal wavefront error (design, manufacturing and alignment), OTA scatter, and detector PSF spread, all of which are maximum at these short wavelengths. Tables 3 and 4 summarize the encircled energy performance within a radius of 0.050" in various UV camera modes. For comparison, values of the HST-only optical PSF encircled energy are shown[5]. The STIS camera mode values, including effects of the detector MTF, are typically >75% of the HST-only values over most of the field.

The lower panels of Figure 6 show a similar montage of log-stretched images across the 52"x52" visible camera field and corresponding horizontal profiles. These unfiltered images show 2x2 pixel (0.10" x 0.10") ensquared energy values of 0.44-0.47 over the field with Gaussian fwhm values of 1.8-2.0 pixels. A long pass filter (F28x50LP) can be inserted to restrict the bandpass to greater than 550nm over a field of 28" x 50"; images acquired in this mode produce identical results to the unfiltered mode. Images of the white dwarf, Feige 34, acquired through the other two available visible filters([OII] - 373nm, [OIII] - 501nm) show 2 x 2 ensquared energy values of 0.50 and 0.47 respectively.

Figure 7 illustrates the effect of OTA breathing on the STIS NUV camera mode. A 2600 second exposure was obtained in time-tag mode of the cluster NGC6681 using the 270nm filter. The upper set of three images, labelled T1, are images of three stars in this field using the initial 520 seconds of data. These images approximately span the detector width as indicated by the pixel locations under each star. The Gaussian fwhm values are marked above and to the left of each image and the encircled energy within a 0.050" radius is indicated above and to the right of each image. The central image is the most compact with the greatest encircled energy, 0.59. The right image is slightly worse, with 0.55 encircled energy. The left image is the worst of the three, with clear horizontal extension and a reduced encircled energy of 0.50. The lower set of three images are the same, corresponding stellar images, obtained 2080 seconds later with the same total 520 seconds exposure time. By this time, defocus from breathing has shifted the focal plane at the STIS detector so that the left and central image are well focused (encircled energies of 0.61 and 0.57 respectively) while the right image is defocused with only 0.43 encircled energy. The detector/focal plane tilt, previously described, causes the sensitivity of the field edges to this defocus; little difference is seen along the field center line as long as the defocus does not exceed the camera depth of field. Similar results have been seen in successive images of the same field and between images of the same field taken several months apart.

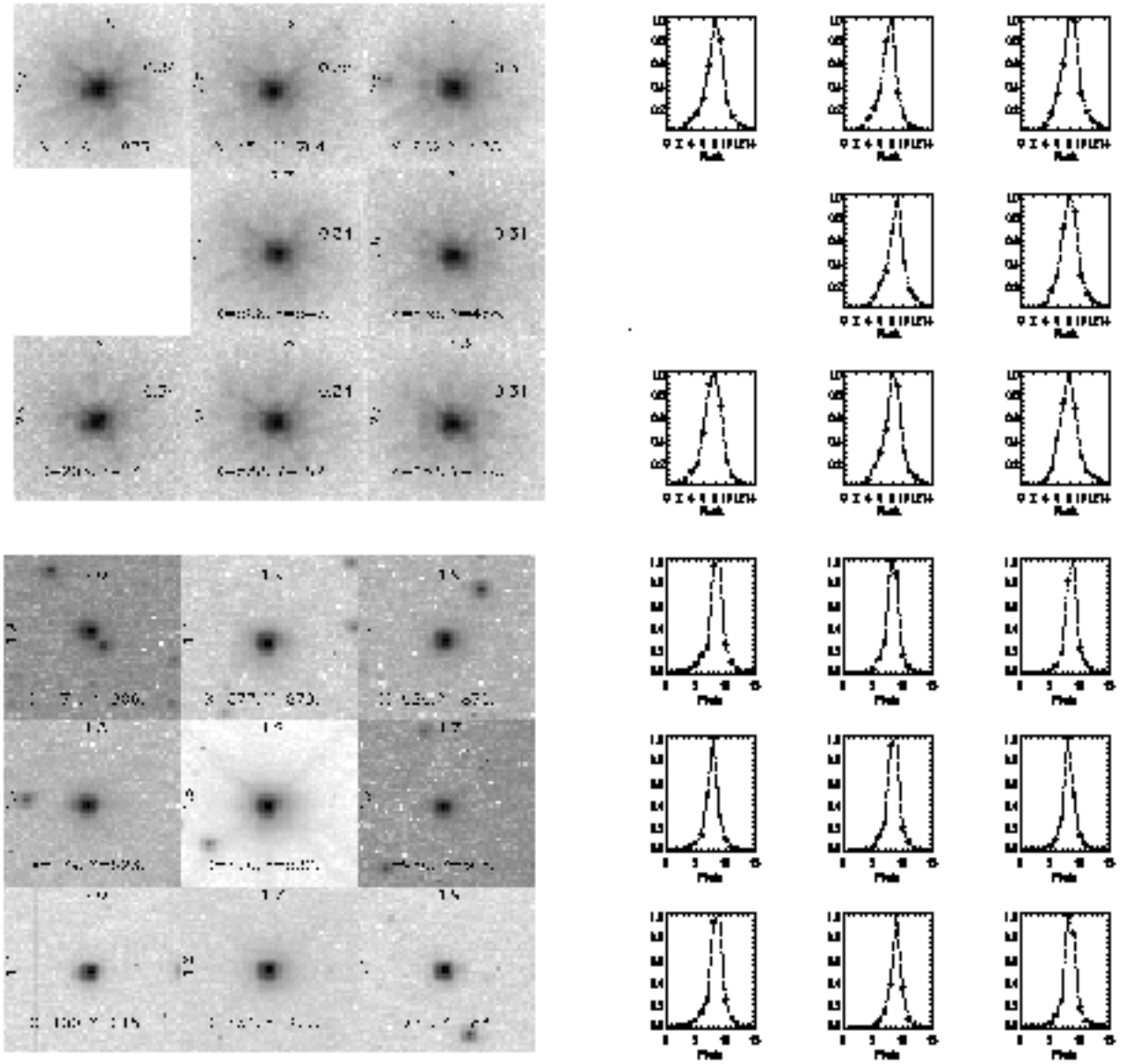

Figure 6. The top, left montage is a log-stretched set of stellar images from an 1100 second exposure of NGC6681 taken with the far-UV MAMA without a filter. Each pixel is about 0.025" with a total field around each star of about 1.3"x1.3" (51 pixels). The Gaussian fit FWHM to vertical and horizontal extracted profiles are given in pixels, to the left and above each star. The encircled energy within a 0.050" radius is indicated to the right and above each image. The flux weighted camera response peaks <130 nm, where STIS residual wavefront error and OTA scatter are greatest. These result in the asymmetric images seen near the corners of the field and the halo around each star. The top, right panel shows horizontally extracted profiles of each star in the field indicating the relative flux distribution. The lower, left panel shows a similar set of stellar images from a 64 second exposure of Omega-Cen acquired with the unfiltered, CCD camera. The plate scale is about twice that of the ultraviolet images, 0.051"/pixel with a 2.6"x2.6" field around each star. Corresponding horizontal, extracted profiles are shown in the adjacent figure. Image quality is generally uniform across the field, with small asymmetries of the PSF most evident in the field corners.

7. CONCLUSIONS

One year after installation, STIS is operating very well with optical performance generally as expected. Following initial corrector alignment, instrument operational checkout, and execution of the basic complement of instrument performance tests, science operations have commenced. In this paper we have tried to summarize the results of some

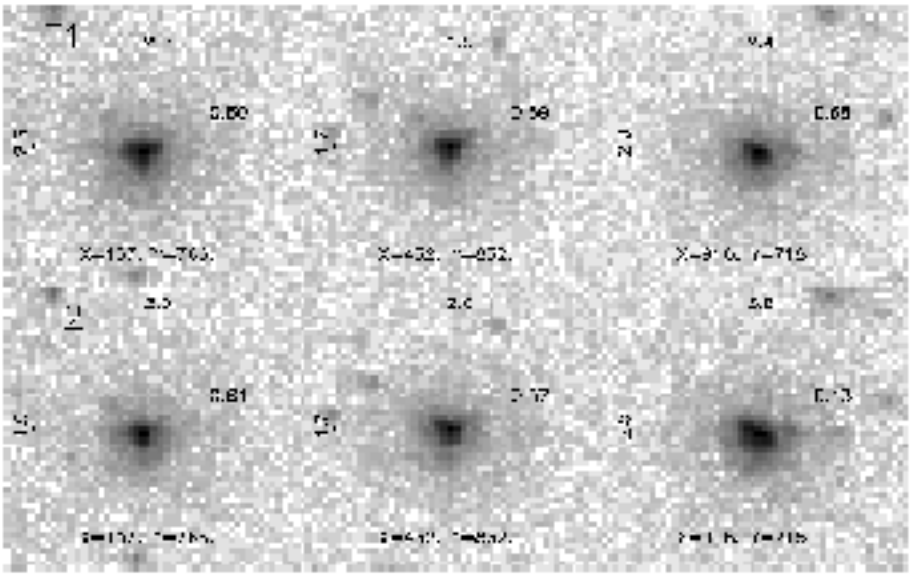

Figure 7. The effects of OTA breathing on the STIS camera modes. The horizontal strips of three images were extracted from a time-tagged image of the cluster NGC6681 using the NUV MAMA with the CN270 filter. The same stars are shown in each horizontal strip with their locations, in pixels, below each. Each exposure was 520 seconds long with 2080 seconds between them. The images are shown log-stretched. The vertical and horizontal Gaussian fwhm, in pixels, are shown to the left and above each image. The encircled energy within a radius of 0.050" is indicated to the right and above each image. The combined effect of the tilt between the detector and focal plane and of OTA breathing is to shift the focal plane across the detector (right to left in the images above) between exposures.

of these intial tests all of which indicate good performance. An ongoing calibration plan is being conducted to more completely describe STIS performance and to monitor the in-flight stability of the instrument. We have reviewed some of the first results of these tests as well; repeated checks of spatial resolution show the range of variation due to OTA breathing to be relatively small, as expected. Finally, we have summarized our progress in providing a robust scatter correction algorithm with very encouraging initial results.

8. ACKNOWLEDGMENTS

The success of the STIS project is due to the combined efforts of many people, through many years, only a few of whom have been specifically named here. Our thanks to them all for an instrument for which they can be proud. The STIS IDT has been funded in response to NASA Announcement of Opportunity OSSA-4-84.

REFERENCES

1. B. E. Woodgate et al., "The Space Telescope Imaging Spectrograph (STIS) Design " *PASP*, submitted, 1998.
2. D. A. Content et al., "Development and testing of diffraction gratings for the Space Telescope Imaging Spectrograph", *Space Telescopes and Instrumentation*, Proc SPIE **2807**, 267, 1996.
3. R. A. Kimble et al., "The On-Orbit Performance of the Space Telescope Imaging Spectrograph", *ApJ*, **492** L83 1998
4. C. W. Bowers, "The On-Orbit Optical Performance of STIS", *The 1997 HST Calibration Workshop*, eds. S. Casertano, R. Jedrzejewski, T. Keyes, & M. Stevens (Baltimore: STScI), 1997.
5. D. J. Schroeder, *Astronomical Optics*, 217, Academic Press, Inc., San Diego, 1987.
6. T. Beck, "STIS MAMA Spectroscopic Mode Image Quality Results", STIS Post-Launch Quick-Look Analysis and SMOV Reports **36**, http://hires.gsfc.nasa.gov/stis/postcal/quick_reports/r036/r036.html, 1997.
7. P. Plait, "SMOV 7077: Spectroscopic Mode Image Quality- CCD ", STIS Post-Launch Quick-Look Analysis and SMOV Reports **36**, http://hires.gsfc.nasa.gov/stis/postcal/quick_reports/r011/r011.html, 1997.
8. K. Sahu, S. Hulbert, H. Lanning, J. Christensen, "Spectroscopic Mode Image Quality of STIS I. First Order Modes", Instrument Science Report **STIS 98-04**, http://www.stsci.edu/ftp/instrument_news/STIS/isrs/stisisr, 1998.
9. D. Lindler, "The Resolution of STIS Mode 1.4 Hi-Res Data Taken with the MAMA Repellor Voltage Off", STIS Analysis Reports,**24**, http://hires.gsfc.nasa.gov/stis/reports/r0024/r0024.html, 1996.
10. J. A. Cardelli, D. C. Ebbets, and B. D. Savage, "Scattered Light in the Echelle Modes of the Goddard High Resolution Spectrograph Aboard the Hubble Space Telescope I.: Analysis of Pre-Launch Calibration Data", *ApJ*, **365** 789 1990
11. J. A. Cardelli, D. C. Ebbets, and B. D. Savage, "Scattered Light in the Echelle Modes of the Goddard High Resolution Spectrograph Aboard the Hubble Space Telescope II.: Analysis of Inflight Spectroscopic Observations", *ApJ*, **413** 401 1993
12. W. Landsman and C. Bowers, "Scattered Light in the STIS Echelle Modes", *The 1997 HST Calibration Workshop*, eds. S. Casertano, R. Jedrzejewski, T. Keyes, & M. Stevens (Baltimore: STScI), 1997.
13. T. R. Gull et al., "STIS on-orbit testing: limiting magnitudes, spectral sensitivity, thermal flexure and MAMA time tagging", *Space Telescopes and Instruments V*, Proc SPIE **3356**, this volume, 1998.
14. R. Robinson, "SMOV Report: Examining the STIS Point Spread Function", STIS Post-Launch Quick-Look Analysis and SMOV Reports **44**, http://hires.gsfc.nasa.gov/stis/postcal/quick_reports/quick_reports.html, 1997.